# Conformational Changes below the $T_m$: Molecular Dynamics Studies of the Thermal Pretransition of Ribonuclease A[†]

Eric D. Merkley,[‡] Brady Bernard,[§] and Valerie Daggett*[,‡,§]

*Department of Biochemistry and Department of Bioengineering, University of Washington, Seattle, Washington 98195-5061*

*Received August 5, 2007; Revised Manuscript Received November 15, 2007*

ABSTRACT: Recent work suggests that some native conformations of proteins can vary with temperature. To obtain an atomic-level description of this structural and conformational variation, we have performed all-atom, explicit-solvent molecular dynamics simulations of bovine pancreatic ribonuclease A (RNase A) up to its melting temperature ($T_m \approx 337$ K). RNase A has a thermal pretransition near 320 K [Stelea, S. D., Pancoska, P., Benight, A. S., and Keiderling, T. A. (2001) *Protein Sci. 10*, 970−978]. Our simulations identify a conformational change that coincides with this pretransition. Between 310 and 320 K, there is a small but significant decrease in the number of native contacts, $\beta$-sheet hydrogen bonding, and deviation of backbone conformation from the starting structure, and an increase in the number of nonnative contacts. Native contacts are lost in $\beta$-sheet regions and in $\alpha$1, partially due to movement of $\alpha$1 away from the $\beta$-sheet core. At 330 and 340 K, a nonnative helical segment of residues 15−20 forms, corresponding to a helix observed in the N-terminal domain-swapped dimer [Liu, Y. S., Hart, P. J., Schulnegger, M. P., and Eisenberg, D. (1998) *Proc. Natl. Acad. Sci. U.S.A. 95*, 3437−3432]. The conformations observed at the higher temperatures possess nativelike topology and overall conformation, with many native contacts, but they have a disrupted active site. We propose that these conformations may represent the native state at elevated temperature, or the N′ state. These simulations show that subtle, functionally important changes in protein conformation can occur below the $T_m$.

A typical free-energy diagram for protein folding shows stable macrostates (native, denatured, and intermediates, if any) as approximately harmonic energy wells along a global reaction coordinate. A more complete picture considers macrostates composed of ensembles of microstates with similar, but not identical, energies and conformations. Expressed differently, the energy landscape is rugged. Simulation studies, alternative conformations in crystal and solution structures, the inactivation of enzymes under folded conditions, and single-molecule enzymology (*1*) demonstrate that the native state is heterogeneous. Microstates are populated according to the Boltzmann distribution. Changing the temperature changes the relative population of conformational microstates with the macrostate. If the average molecular conformation varies with temperature, the observable properties of the native state will also vary with temperature. This is one possible explanation for the sloping baselines frequently observed by many spectroscopic probes of protein folding (*2*).

Recent experimental (*3*) and simulation (*4*) studies support the existence of a distinct native state at elevated temperature, or the N′ state. The N′ state retains highly nativelike topology and tertiary contacts, although it is expanded and less tightly packed than the native state (*4*). More subtle structural features, such as those necessary for biological activity, may be lost. The nature of the N′ state can be described in two fundamentally different ways using the energy landscape model of protein folding. First, the N′ state may simply be the population profile of conformational microstates that exists at elevated temperature, as described above. Second, instead of a shift in the populations of microstates, the position of the native basin (macrostate) in conformational space may shift. The N′ state would arise as the position of the native state minimum on the free energy landscape changes with temperature. Leeson et al. (*3*) used this description of the N′ state to model the nonexponential folding kinetics of cold shock protein A in temperature-jump experiments.

To probe the variation in structural properties within the native state, we have performed molecular dynamics (MD)[1] simulations of bovine pancreatic ribonuclease A (RNase A). RNase A is one of the best studied of all proteins, and it has served as a model for protein folding and enzyme function for decades. Its three-dimensional structure has been determined by neutron diffraction (*5*), NMR (*6*), and X-ray

[†] This research was supported by National Institutes of Health Grant GM50789 (to V.D.) and Molecular Biophysics Training Grant 5 T32 GM008268-19 (to E.D.M.).

* To whom correspondence should be addressed. E-mail: daggett@u.washington.edu. Phone: (206) 685-1510. Fax: (206) 685-3300.

[‡] Department of Biochemistry.

[§] Department of Bioengineering.

[1] Abbreviations: RNase A, bovine pancreatic ribonuclease A; MD, molecular dynamics; FTIR, Fourier transform infrared spectroscopy; 2D FTIR, two-dimensional Fourier transform infrared correlation spectroscopy; CD, circular dichroism spectroscopy; NMR, nuclear magnetic resonance spectroscopy; UV, ultraviolet; F3C, flexible three-center computational water model; PDB, Protein Data Bank; $C_\alpha$ rmsd, root-mean-square deviation of $C_\alpha$ atom coordinates from the starting structure; $C_\alpha$ rmsf, root-mean-square fluctuation of $C_\alpha$ atom coordinates about the average structure; NOE, nuclear Overhauser effect; $T_m$, transition temperature for protein unfolding; SASA, solvent-accessible surface area; CI2, chymotrypsin inhibitor 2.

10.1021/bi701565b CCC: $40.75 
Published on Web 12/28/2007

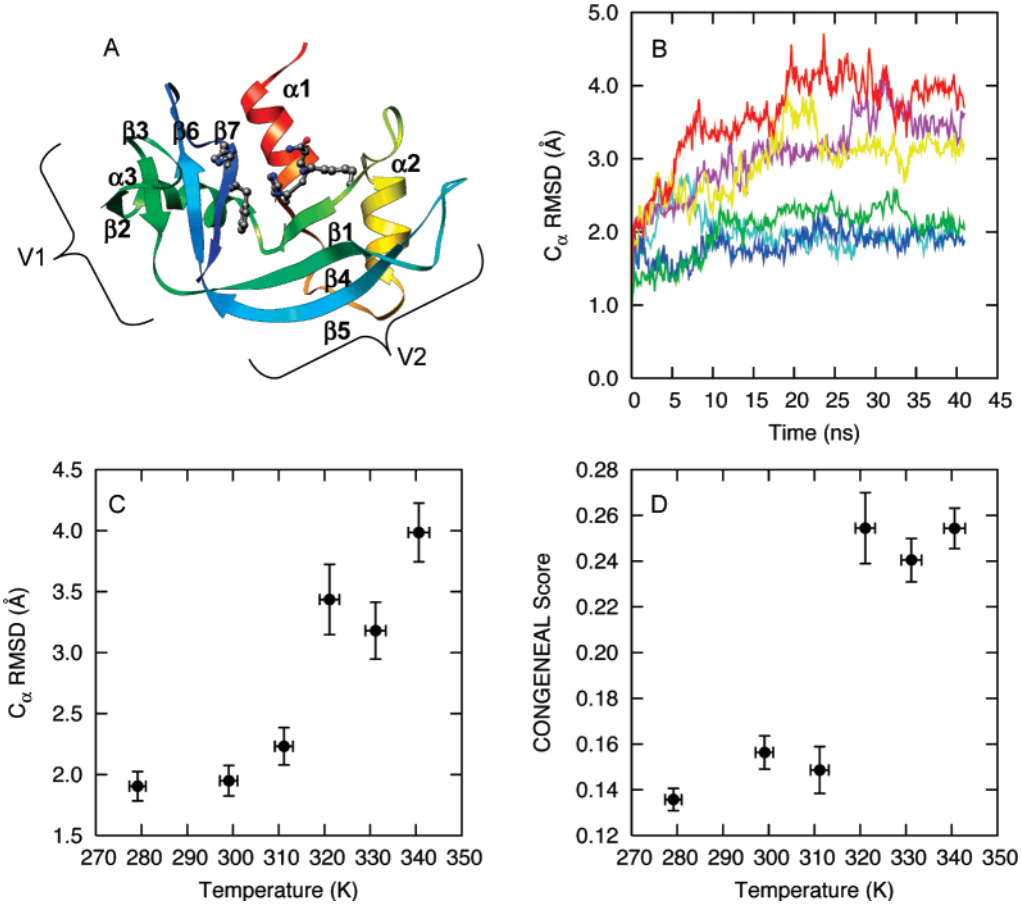


FIGURE 1: Deviation of RNase A during MD simulations. (A) Structure of RNase A (Protein Data Bank entry 1kf5) in ribbon representation, colored from red at the N-terminus to blue at the C-terminus. Secondary structure elements are labeled, and active site residues Gln 11, His 12, Lys 41, His 119, and Phe 120 are shown in ball-and-stick representation. (B) $C_\alpha$ rmsd as a function of time: cyan, 278 K; blue, 298 K; green, 310 K; magenta, 320 K; yellow, 330 K; and red, 340 K. For clarity, the data have been smoothed over a 100 ps sliding window. (C) Average $C_\alpha$ rmsd from the starting structure. (D) Average CONGENEAL dissimilarity scores (*42*) with respect to the starting structure. For panels C and D, the values shown are averages of data over 20−41 ns. The temperature values are averages over the same time period. Horizontal error bars represent one standard deviation in temperature.

crystallography (e.g., ref *7*; there are more than 70 structures of RNase A in the Protein Data Bank). RNase A is a 124-amino acid monomeric protein containing four disulfide bonds. The structure consists of two lobes, each containing a $\beta$-sheet and a helix that packs against it, with the N-terminal helix (α1) partially filling the cleft between the two lobes (Figure 1A). This cleft contains the active site.

The thermal unfolding of RNase A has been studied by differential scanning calorimetry (*8*−*12*), nonspecific photochemical surface labeling (*13*), circular dichroism (*14*) (and references in ref *15*), Fourier transform infrared (FTIR) (*9*, *15*−*19*), Raman (*20*), and UV spectroscopy (*14*, *21*), NMR (*22*, *23*), and limited proteolysis (*14*, *15*, *21*). All of these techniques identify the major unfolding transition of RNase A to be in the range of 334−337 K near neutral pH. The folding of RNase A is not strictly two-state; a minor thermal transition, termed the pretransition, occurs at ~320 K (*9*, *16*−*19*). The spectroscopic evidence for the pretransition is subtle, and not all spectroscopic probes identify the pretransition. For example, Stelea et al. (*9*) did not detect the pretransition by single-wavelength monitoring of the IR amide I′ band or by CD in the near- or far-UV region. However, principal component analysis of their FTIR and far-UV CD data can detect it (*9*). Similarly, 2D FTIR correlation techniques (*16*−*19*) also detect the pretransition. The pretransition temperature coincides with the onset of the loss of enzymatic activity (*21*).

These studies have led to several structural models of the pretransition. The model of Burgess and Scheraga, later modified by Matheson and Scheraga (*13*, *15*), proposed six partially overlapping stages of unfolding: a change in the environment of Tyr 92 (stage 1, 308−323 K), pulling away of the α1−α2 loop (stage 2, 303−313 K), unfolding of α2 and the $\beta$3−$\beta$4 loop (stage 3, 313−323 K), unfolding of α3 and C-terminal strands 6 and 7 (stage 4, 323−333 K), unwinding of α1 (stage 5, 328−338 K), and, finally, unfolding or partial unfolding of the remainder of the structure, including the $\beta$-strands and the surrounding loops (stage 6, 333−343 K) (*13*). Stages 1−4 are the most relevant to the pretransition. On the basis of their CD and FTIR data, and previous hydrogen exchange studies that identified the $\beta$-sheet and α3 as the most stable regions (*12*, *24*), Stelea et al. (*9*) proposed that the C-terminal portion of α2 begins to unfold just above 298 K. This unfolding, in turn, is proposed to destabilize the adjacent $\beta$1, which might then begin to unfold around 308 K. Recent studies have used FTIR and various 2D correlation techniques (*18*, *19*) to study RNase A unfolding, with the consensus that the first secondary structure element to unfold as the temperature is increased is strongly hydrogen-bonded $\beta$-sheet, followed by helix,

followed by more weakly hydrogen-bonded $\beta$-sheet. In general agreement with Stelea et al. (*9*), Zhang et al. (*18*) concluded that changes in the N-terminal region during the pretransition expose the core to solvent and lead to further unfolding. The authors of another 2D FTIR study (*17*) concluded that two populations of $\beta$-sheet unfold sequentially in the narrow temperature range of the pretransition. Thus, the pretransition itself is also a non-two-state process. This idea is in accord with the early scheme of Burgess and Scheraga in describing the unfolding of RNase A as a series of partially overlapping structural changes.

The MD simulations described here at six temperatures from 278 to 340 K provide an opportunity to model the structural changes that occur below and near the $T_m$. RNase A and its domain-swapped dimers have been the subject of previous MD simulations (*25*−*34*). These simulations have provided important insights into several aspects of RNase A structure and function, such as the relationship between correlated motion and the various ligand- and pH-dependent conformations observed in experimental structures (*26*, *29*) and the role of these correlated motions in the domain-swapped dimers (*25*, *27*), solvation (*30*, *31*), changes in dynamics and conformation upon ligand binding (*29*, *32*, *33*), and unfolding (*34*). However, this work is the first attempt to simulate RNase A across temperatures up to the $T_m$ and on the time scale of tens of nanoseconds. By analyzing secondary structure, intramolecular contacts, and a variety of other structural properties, we are able to detect a significant conformational change between 310 and 320 K. This change is largely localized to $\alpha$1, $\beta$1, and $\beta$7, but the buried faces of the other two helices, $\beta$-strands 2, 3, and 6, and loop regions also participate. Since the native topology and contacts are largely preserved, and since the pretransition is a gradual change rather than a two-state process, these altered conformations may represent the native state of RNase A at elevated temperature (N′).

## METHODS

*Molecular Dynamics Simulations and Analysis.* The starting model for MD simulations was the 1.15 Å resolution crystal structure of phosphate-free bovine pancreatic ribonuclease A at pH 7.1 [PDB entry 1KF5 (*7*)]. We performed six simulations, one each at 278, 298, 310, 320, 330, and 340 K. All of these simulations were conducted at neutral pH (Asp, Glu, Arg, and Lys ionized). His 12 and 48 were protonated at ND1, and His 105 and 119 were protonated at NE2. His tautomers were assigned on the basis of examination of electron density maps and electrostatic and hydrogen bonding interactions (*7*, *35*). For residue 12, the electron density as a function of pH shows that the proton at NE2 is labile, whereas the ND1 proton is stable (*35*). His 105 was assigned to the NE2 tautomer by default. These tautomer assignments are the same as those used previously in our simulation studies of RNase A at neutral pH (*34*) and those used by Merlino et al. (*26*).

MD simulations were performed using the *in lucem* molecular mechanics program (*il*mm) (*36*) with the flexible three-center water model (F3C) (*37*). The potential energy function and simulation protocols have been described previously (*36*, *38*). A force-shifted nonbonded cutoff of 10 Å was used, and the nonbonded list was updated every three steps.

Table 1: Target Simulation Temperatures, Experimentally Derived Water Densities (*40*, *41*), and the Simulation System Densities

| T (K) | water density (g/cm$^3$) | system density (g/cm$^3$) |
|---|---|---|
| 278 | 0.999965 | 1.045866551 |
| 298 | 0.997000 | 1.043032900 |
| 310 | 0.993000 | 1.039210100 |
| 320 | 0.989400 | 1.035769580 |
| 330 | 0.984700 | 1.031277790 |
| 340 | 0.979500 | 1.026308150 |

The starting structure was minimized for 1000 steps of steepest descent minimization in vacuo. The protein was then solvated in a box of F3C waters pre-equilibrated to a temperature at which the solvent density was near the desired density for the target temperature (Table 1). The solvent density was calculated by subtracting the volume of the protein from the volume of the simulation box. Protein volume was calculated by the Voronoi procedure (*39*) for the average protein volume from a 2 ns simulation at each temperature. Finally, the system density was set to achieve the experimental density of water for each desired temperature (*40*, *41*). System and water densities are given in Table 1. The solvent was then minimized (1000 steps), followed by 1 ps of water-only dynamics and then another 500 steps of minimization of water only. Finally, the entire system was minimized for 500 steps. Following this solvation protocol, we heated the system to the desired temperature by assigning equal and opposite initial velocities to randomly selected pairs of atoms until the velocities of the system satisfied the Maxwell distribution for that temperature. Simulations were performed for 41 ns.

Analysis of MD simulations was also carried out with *il*mm, with averages taken over 20−41 ns of each simulation. The root-mean-square deviation of $C_\alpha$ atoms from the starting structure ($C_\alpha$ rmsd) and rms fluctuations of $C_\alpha$ atoms from the average structure over 20−41 ns ($C_\alpha$ rmsf) were calculated. The $C_\alpha$ rmsf values for crystal structures were estimated from the crystallographic *B*-factors, as rmsf = $(3B/8\pi^2)^{1/2}$. The CONGENEAL dissimilarity score of Yee and Dill was used to compare structures to the starting conformation (*42*). For two proteins, *R* and *S*, the dissimilarity score $d(R,S)$ is given by

$$d(R,S) = \frac{\sum_{i=1}^{N-2}\sum_{j=i+2}^{N} |r_{ij}^{-2} - s_{ij}^{-2}|}{\frac{1}{2}\left(\sum_{i=1}^{N-2}\sum_{j=i+2}^{N} r_{ij}^{-2} + \sum_{i=1}^{N-2}\sum_{j=i+2}^{N} s_{ij}^{-2}\right)}$$

where $r_{ij}$ and $s_{ij}$ are the distances between $C_\alpha$ atoms of residues *i* and *j* in proteins *R* and *S*, respectively.

Interatomic heavy-atom contacts were counted according to the following definition: carbon atoms ≤5.4 Å apart and any other pair of non-hydrogen atoms ≤4.6 Å apart. Residues were considered to be in contact if any interresidue pair of atoms was in contact. Contacts were additionally classified as salt bridges (Glu or Asp and Arg, Lys), hydrogen bonds (donor−acceptor angle greater than 135° and a hydrogen−acceptor distance of ≤2.6 Å), hydrophobic contacts (C−C distance between $CH_n$ groups of ≤5.4 Å), or "other" contacts (not fitting any other definition). When a contact fit both

the salt bridge and the hydrogen bond criteria, it was counted as a salt bridge.

To compare the number of native contacts between simulations on a per-residue basis, we calculated a quantity that we call the contact density. In a static structure, the contact density for residue *i* is the number of residues that contact that residue. The same calculation can be done for a simulation-averaged contact map, with each contact's contribution weighted by the percentage of time it is present. The difference native contact density is the difference between the contact density in the starting structure and the simulation-averaged value. This quantity is equivalent to the average number of native residue−residue contacts lost during the simulation.

The simulations were compared to the solution NMR data (*6*). NOE-derived distance restraints were considered satisfied if they met the following criterion:

$$\left(\frac{1}{N}\sum_i r_i^{-6}\right)^{-1/6} \leq r_{\mathrm{UB}}$$

where $r_i$ is the distance between a given pair of protons at time $t_i$ in the simulation, $N$ is the number of time points, and $r_{\mathrm{UB}}$ is the experimental upper bound restraint distance or 5 Å, whichever is greater. Two sets of NOEs have been presented, with different conformations for His 105 and His 119 (*6*). To calculate the percentage of satisfied NOE restraints, the first set was used unless it was violated, in which case the second set was considered. In calculating NOE restraint satisfaction, we considered structures from 20 to 41 ns.

Side chain dihedral angle order parameters $O_\chi$ were calculated from the simulations as described by Wong and Daggett (*43*). We calculated $O_{\chi_1}$ for all residues having a $\chi_1$ angle except Ala (the rotation of the methyl side chain is essentially unrestricted). For calculating $O_{\chi_2}$, we additionally excluded valine for similar reasons and cysteine due to disulfide bonds. Secondary structure assignments were done with the algorithm of Kabsch and Sander (*44*) with additional definitions from Scouras and Daggett (*65*), implemented in *il*mm. Solvent-accessible surface areas (SASAs) were calculated by the method of Lee and Richards (*45*). Protein structure graphics were prepared with the Chimera software package from the Resource for Biocomputing, Visualization, and Informatics at the University of California, San Francisco (supported by NIH Grant P41 RR-01081) (*46*).

## RESULTS AND DISCUSSION

*Global Conformational Properties of RNase A as a Function of Temperature. (i) Comparison with Experimental NOE Restraints.* We have compared the simulations to the experimental NOE restraints (*6*). The fractions of total NOE restraints satisfied for the six simulations were as follows: 91% at 278 K, 93% at 298 K, 94% at 310 K, 86% at 320 K, 85% at 330 K, and 83% at 340 K. At 278 K, the NOE violations are localized to $\beta$-strands 2 and 7 and some residues in $\beta$-strands 4 and 5. The simulations at 298 and 310 K are similar, but with fewer violations in $\beta$7 and fewer overall. At the three highest temperatures, where structural perturbations may be expected, NOE restraints are violated largely in the same regions but to a greater extent. The mean violation distance for the three lowest temperatures was ∼1 Å.

The minimized starting structure satisfies 96.1% of the experimental restraints. The NOE analysis illustrates that the native topology and contacts of the protein are well-preserved in all of the simulations, even at high temperatures. The NMR experiments were conducted at 308 K and pH 4 in the presence of saturating concentrations of phosphate ion (*6*). Interestingly, the best agreement between simulation and experiment is for the 310 K simulation, the simulation closest to the experimental temperature. For comparison, we conducted simulations of RNase A with a phosphate ion bound in the active site (phosphate ion coordinates were taken from ref *47*, PDB entry 5RSA) at neutral pH (11 ns) and low pH (5.9 ns). These simulations satisfied 93 and 92% of the experimental restraints, respectively. Structures from the NMR ensemble satisfy an average of 97.9 ± 0.3% of the restraints; the 1KF5 crystal structure satisfies 97%. Therefore, pH- and ligand-induced differences in RNase A conformation are small, but more extensive sampling (longer and more simulations) is needed for improved comparison with the experimental NOEs.

*(ii) Conformational Properties.* Figure 1B shows the $C_\alpha$ rmsd from the starting structure over time for the six 41 ns simulations of apo RNase A up to its $T_m$. The asymptotes at long times suggest that all the trajectories equilibrate within ∼20 ns. Figure 1C shows the average $C_\alpha$ rmsd for each temperature (averaged over 20−41 ns of each simulation). These data indicate that the six simulations fall into two groups, low temperature and high temperature, with the transition occurring between 310 and 320 K. For the first group (278, 298, and 310 K), the highest observed $C_\alpha$ rmsd is ∼2.7 Å. These deviations are slightly higher than those seen in some other MD studies of RNase A, possibly due to the ∼10-fold shorter time scale of some of these studies (*26*, *28*, *29*); our Cα deviations at the lower temperatures are similar to those seen in the longer simulation of Sanjeev and Vishveshwara (*30*). The 278 K simulation experiences a large change initially, reaching ∼2.7 Å from the starting structure, and then returns to conformations ∼2 Å from the starting structure by 10 ns. The simulations in the second group (320, 330, and 340 K) reach higher maximum $C_\alpha$ rmsd values (∼3−5 Å). These higher-temperature conformations are not globally unfolded, and very nativelike topology is preserved. For comparison, conformations from previous high-temperature (498 K) MD simulations of RNase A reached a $C_\alpha$ rmsd of 15−20 Å (*34*).

Measurements of some key active site distances in our simulations show preservation of the His 12 ND1···Thr 45 backbone oxygen hydrogen bond and loss of the hydrogen bond between His 119 and Asp 121, in keeping with the simulation study of Merlino et al. (*26*). Also as in their study, at 278 and 298 K, we see rare formation of a hydrogen bond between the Thr 45 and Asp 83 side chain (data not shown), which is present in crystal structures only when a uridine base is bound to the active site (*26*, *48*; see also references in ref *49*).

We have also calculated the average CONGENEAL dissimilarity score (*42*) for each simulation relative to the starting structure (Figure 1D). This score, which is sensitive to local arrangements of secondary structure elements, measures the dissimilarity between two structures by com-

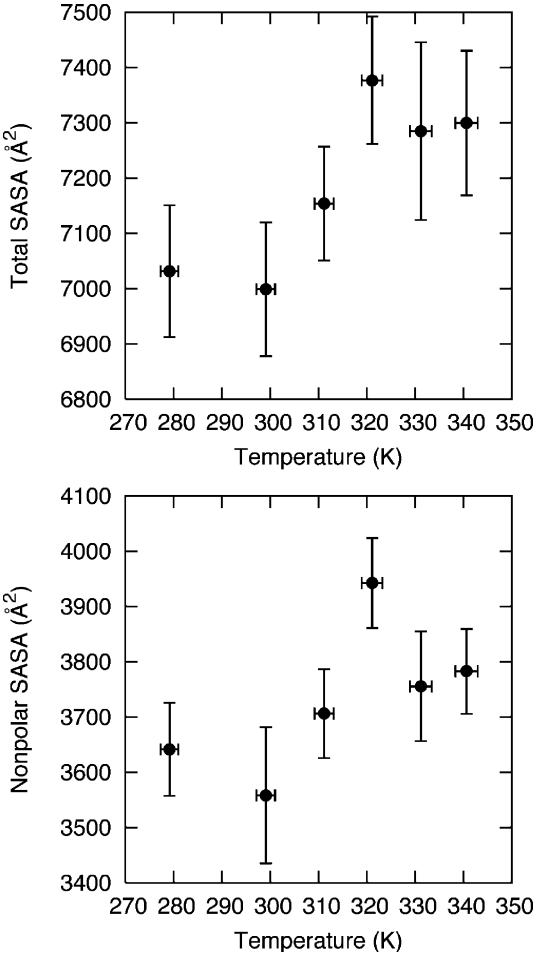


FIGURE 2: Solvent-accessible surface areas (SASAs) of RNase A during MD: (A) total SASA and (B) nonpolar SASA. Vertical error bars represent one standard deviation. Horizontal error bars represent one standard deviation in temperature, averaged over the same time period.

paring their weighted distance matrices. The higher the score, the more dissimilar the structures. Like the $C_\alpha$ rmsd, the CONGENEAL score identifies an abrupt increase in dissimilarity to the starting structure between 310 and 320 K.

The average solvent-accessible surface area [SASA (Figure 2A)] of RNase A increases from ~7040 Å$^2$ at 278 K to ~7280 Å$^2$ at 320 K, a change of ~3.5%, and it is approximately constant from 320 to 330 K. As with $C_\alpha$ rmsd and the CONGENEAL score, the greatest change occurs around 310 K. However, the fluctuations in SASA (~1−4%) are similar in magnitude to the variation in SASA with temperature, and a linear trend is sufficient to describe the data. The average nonpolar SASA (Figure 2B) also increases with temperature and has large fluctuations. Given that RNase A does not globally unfold in our simulations, these small changes in total and nonpolar SASA seem reasonable.

*(iii) Contact Analysis.* To examine intramolecular interactions, we calculated the numbers of salt bridges, hydrogen bonds, nonpolar contacts, and "other" contacts. The number of intraprotein hydrogen bonds is approximately constant within the uncertainty, dropping off only slightly with an increase in temperature (Figure 3A). The number of intraprotein hydrophobic contacts drops slightly, between 310 and 320 K (Figure 3B). The number of other intraprotein contacts is stable at lower temperatures but starts to drop off at

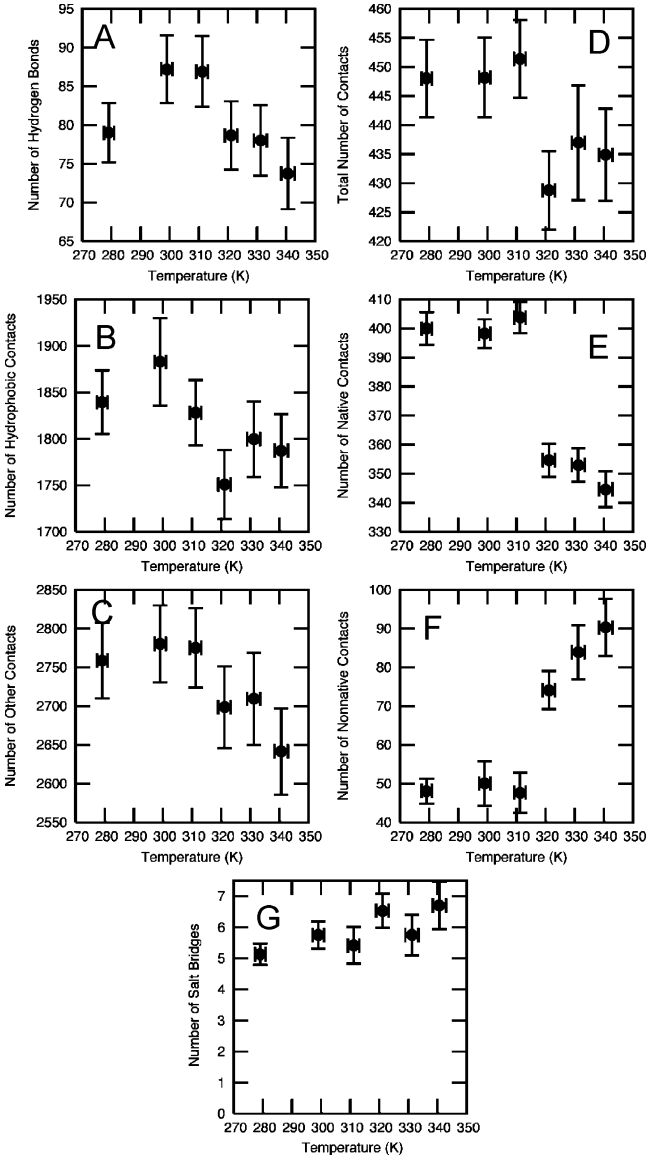


FIGURE 3: Contact analysis of RNase A during MD. (A) Number of hydrogen bonds. (B) Number of hydrophobic contacts. (C) Number of contacts that are not hydrogen bonds or hydrophobic contacts. Panels A−C show contacts on an atom−atom basis. (D) Total contacts. (E) Native contacts. (F) Nonnative contacts. (G) Salt bridges. Panels D−F show contacts calculated on a residue basis. Note the obvious discontinuity in panels D−F between 310 and 320 K. All values are averages over 20−41 ns. Error bars represent one standard deviation.

320 K (Figure 3C). The number of salt bridges increases approximately linearly with temperature (Figure 3G). The large error bars in Figure 3A−C,G mean that these trends are not statistically significant. Still, the observed changes occur at the same temperature as statistically significant changes in other properties (see above). When the intraprotein residue contacts are classified as native or nonnative, a clearer picture emerges. In the pretransition temperature range, the number of native contacts decreases by 12.5% and the number of nonnative contacts increases by 70% (Figure 3D,F). The opposite trends in the number of native and nonnative contacts lead to a very small change (~3.5%) in the total number of contacts.

*(iv) Global Levels of Secondary Structure.* Overall, the secondary structure elements of RNase A are stable at the

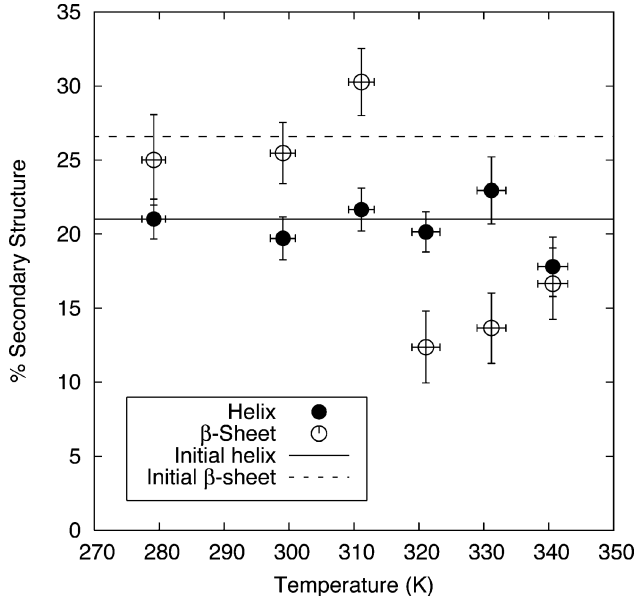


FIGURE 4: Secondary structure assignments for RNase A MD. The data shown are the average percentages of residues in the indicated type of secondary structure from 20 to 41 ns.

lower temperatures (Figures 4 and 5). The content of α-helix remains essentially constant up to 340 K. However, almost half of the $\beta$-sheet structure is lost in the 320−340 K simulations. The Kabsch and Sander algorithm (*44*) used for these calculations identifies secondary structure by hydrogen bond patterns. An analysis based on $\phi$ and $\varphi$ angles (not shown) does not detect the drop in $\beta$-sheet content because the sheet residues largely remain in the $\beta$ Ramachandran bin.

The results above for $C_\alpha$ rmsd, CONGENEAL dissimilarity score, $\beta$-sheet hydrogen bonding patterns, and native and nonnative intraprotein contacts suggest a conformational change between 310 and 320 K. The changes in these structural properties are distinct, but not large. Similar suggestive, but not statistically significant, trends are seen in SASA and the number of hydrogen bonds, hydrophobic contacts, and other (polar−nonpolar) contacts. The temperature range of this structural change coincides with the experimental pretransition temperature. We now turn to a description of the conformational changes that lead to these observed changes in structural properties.

*Temperature-Induced Conformational Changes of RNase A. Secondary Structure. (i) Dynamics of Secondary Structure Elements.* To examine the conformational changes that occur in the temperature range of the thermal pretransition, we first explore the stability of the secondary structure elements. We then analyze the same conformational change in terms of interresidue contacts. The time-averaged global analysis shown in Figure 4 hides both the dynamic nature of the secondary structure and the differences between individual secondary structure elements. To obtain a more detailed picture, we assigned secondary structure as a function of time and residue number (Figure 5). In the simulations at 278, 298, and 310 K, α1 remains well-formed and stable and intermittently gains an additional residue at the C-terminus. α2 is also stable and gains two additional residues of $\pi$-helix at the C-terminus. In α3, the four C-terminal residues (Ala 56−Ser 59) fluctuate between α-helical and $3_{10}$-helical conformations. These fluctuations are minor rearrangements of hydrogen bonds within the helix, and the occasional involvement of Gln 60 in α-helical structure does not appear to perturb the adjacent $\beta$2.

The $\beta$-sheet structure is also stable at the three lowest temperatures, although there are local deviations from regular structure. For instance, the N-terminus of $\beta$1 (residues 42−44) loses its hydrogen bonds to $\beta$4 (residues 83 and 84), and the two strands pull apart. Residues 83−85 on $\beta$4 also lose hydrogen bonds to $\beta$5 (residues 98−100). The loss of native hydrogen bonds near the presumably stabilizing disulfide bond is surprising. However, this disulfide promotes local disruption of the $\beta$-sheet by coupling its fluctuations to those of α2 and the α1−α2 loop. $\beta$4 and $\beta$5 do not pull apart, possibly because the Cys 26−Cys 84 disulfide linkage serves to hold $\beta$4 in place in the absence of regular $\beta$-sheet hydrogen bonding, or possibly because of other well-maintained hydrogen bonds between the strands. The role of the Cys 26−Cys 84 disulfide in the dynamics of the $\beta$-sheet warrants further investigation, ideally via comparison with simulations of the reduced protein. Interestingly, the $\beta$-sheet is better formed at 310 K than at 278 or 298 K.

At the higher temperatures, the stability of the secondary structure elements changes (Figure 5). At 320 K, the native helical structure is stable. The $\beta$-sheets are significantly more disrupted than at lower temperatures, with hydrogen bonding between $\beta$1 and $\beta$4 and between $\beta$2 and $\beta$3 almost completely absent. Hydrogen bonding between $\beta$3 and $\beta$4 is lost by ∼26 ns. Even though hydrogen bonds are lost, the strands generally maintain beta $\phi$ and $\varphi$ angles. We speculate that at high temperature, the Cys 26−Cys 84 and Cys 40−Cys 95 disulfide bonds restrict the position of $\beta$-stands 1, 4, and 5 and contribute to the preservation of native topology in spite of the loss of regular hydrogen bonding. At 330 and 340 K, the $\beta$-sheets are even more extensively disrupted, especially $\beta$6 and $\beta$7. However, at these temperatures, $\beta$2 and $\beta$3 maintain their native hydrogen bonds, in keeping with hydrogen exchange data (*12*). The C-terminus of α3 is frayed at 330 K, and at 340 K, the helical hydrogen bonding pattern is almost completely disrupted.

Although several experimental studies suggest that there is some loss of helical structure during the pretransition (∼320 K), we do not see significant loss of helical structure until 340 K. It is possible that this finding is due to the short time scale of our simulations. However, we do observe loss of $\beta$-structure, particularly in the first and last strands of the $\beta$-sheet, in agreement with the general conclusions of recent FTIR studies (*9*, *18*, *19*) that some $\beta$-structure is lost during the pretransition. Our simulation results allow us to propose that these changes are localized primarily to $\beta$1 and $\beta$7. Changes in α2 followed by $\beta$1 in the pretransition were proposed by Stelea et al. (*9*), and unfolding of $\beta$6 and $\beta$7, as well as α3, is in keeping with stage IV (323−333 K) of the Burgess−Scheraga model (*15*).

*(ii) Formation of a Nonnative Helix.* In the simulations at 330 and 340 K, a nonnative helix (designated helix NN) is formed between residues 15 and 20, which correspond to the α1−α2 loop in the native structure (Figure 5). Helix NN is formed earlier and is more stable at 340 K than at 330 K. The new helix packs against α1 and $\beta$1, $\beta$4, and $\beta$5, with extensive repacking of side chains (Figure 6). The native Asp 14···Tyr 25 hydorgen bond is broken intermittently in

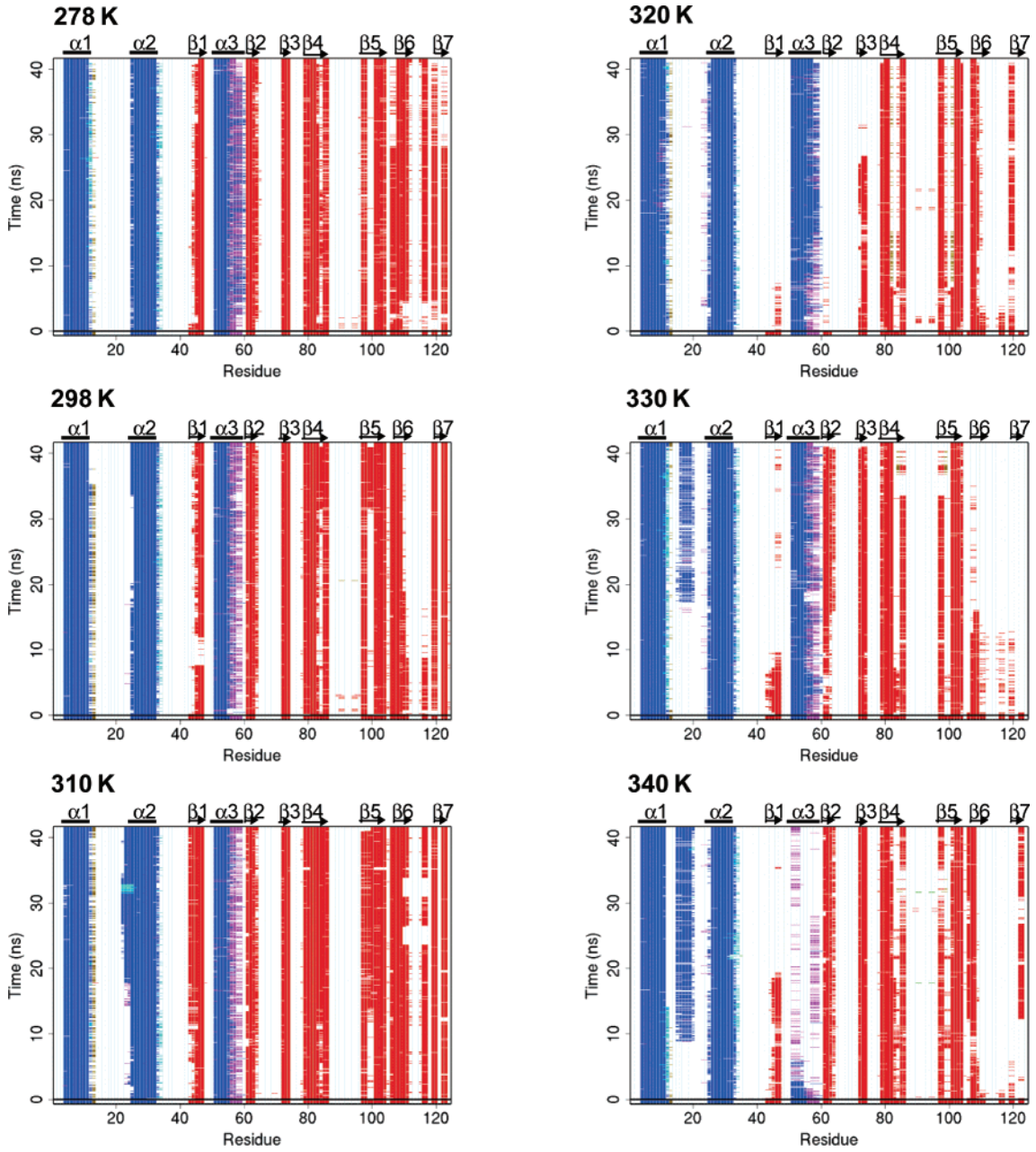


FIGURE 5: Secondary structure assignments for RNase A MD. The horizontal axis of each plot gives the residue number and the vertical axis time, and the color indicates secondary structure assignment at the given time point: blue, α-helix; red, $\beta$-sheet; cyan, $\pi$-helix; magenta, $3_{10}$-helix; brown, mixed α- and $\beta$-sheet; and green, α-bridge (*44*, *65*). The negative time axis indicates the starting conformation.

the simulations (lower left of Figure S1 of the Supporting Information). The Tyr 25 side chain becomes more exposed to solvent at the four highest temperatures (not shown). The formation of helix NN shortens the loop joining α1 and α2, which is related to the movement of α1 away from the core (Figure 8) and the change in the angle of α2 (Figure 6), which may, in turn, lead to further changes in the $\beta$-sheet. AGADIR (*50*−*54*) predicts low (∼1%) helical propensity in this region, suggesting that tertiary interactions are largely responsible for forming helix NN. Flickering residual helical structure was observed in this region in high-temperature unfolding simulations (*34*). More importantly, this helix is present in one of the monomers of the N-terminal domain-swapped dimer (*55*), which is formed under conditions of low pH, high temperature, or organic solvents (*56*). Alignment of the final structure from the 340 K simulation with one of the functional units of the domain-swapped dimer shows the relationship of the two conformations of helix NN (Figure 6).

Observation of a nonnative helix in a high-temperature MD simulation of RNase A does not mean that conformations with this nonnative helix make up a large proportion of the experimental ensembles. However, simulation and experiment agree that this region is capable of forming helix under certain conditions. It appears that our simulations capture some of the forces at work under the experimental conditions where the nonnative helix is observed (*56*). In fact, the simulated conformations containing nonnative helix might provide an indication of the pathway to the N-terminal domain-swapped dimer. In earlier MD simulations (*34*), α1 became completely detached from the main core of the protein at both neutral and low pH, leading to conformations


FIGURE 6: Structure of the nonnative helix formed during MD at 340 K. (A) Structure of the N-terminal domain-swapped dimer, 1A2W (*55*). The monomer (in gray) exhibiting a nonnative helix (residues 15−20 colored red) with the other monomer colored blue. (B) Final structure from the 340 K MD simulation colored yellow with residues 15−20 colored red. (C) Superposition of the N-terminal domain-swapped dimer and the final, 340 K MD snapshot. The coloring is the same as in panels A and B. The MD structure was aligned by $C_\alpha$ atoms to the upper right functional unit.

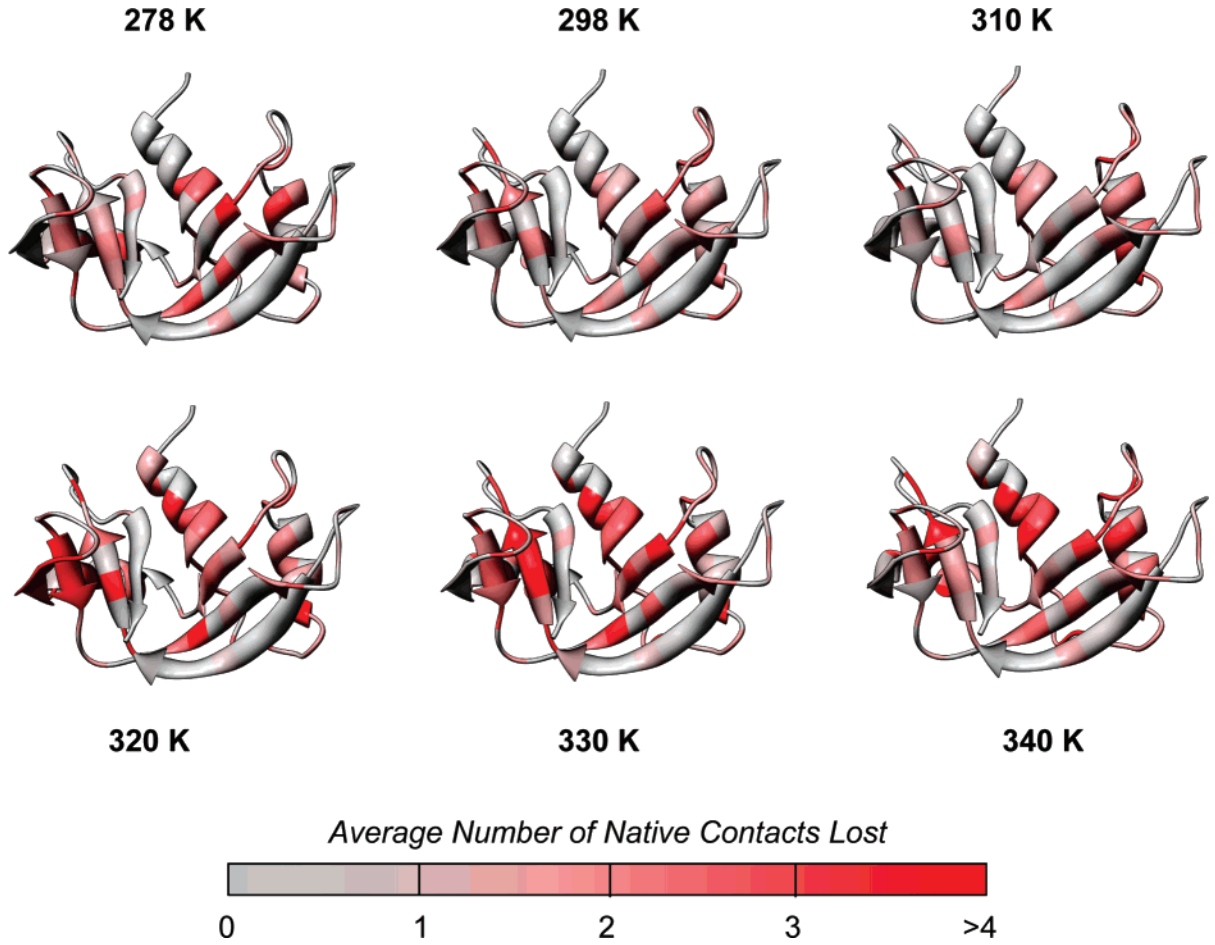


FIGURE 7: Difference contact density plotted onto the RNase A structure. Difference contact density for a given residue is equivalent to the average number of native contacts lost by that residue during the simulation. The color scale spans the range from 0 (gray) to 4 (red). The eight residues with a difference contact density of >4 (4.13−6.39) are also colored red.

similar to the N-terminal domain-swapped dimer with the same transient nonnative helix (residues 15−22). At neutral pH, nonnative helix formation was linked to a further movement of the N-terminus away from the core. In this work, α1 also moves away from the β-sheet, but not as far. The conformations in our simulations at 330 and 340 K seem poised for a further dissociation or "undocking" of α1 from the β-sheet, which might allow straightening of the α1-helix NN turn and extension of the nonnative helical structure, leading to a closer match with the domain-swapped dimer (Figure 6).

The importance of the NN helix and dissociation and/or fluctuation of α1 along the pathway to the N-terminal domain-swapped dimer has been challenged, however. The highly homologous bovine seminal ribonuclease also forms a domain-swapped dimer by exchanging α1 (*57*, *58*), and no helical structure is present in the hinge region of this dimer (residue 19 is a proline). Further, although the hinge peptide

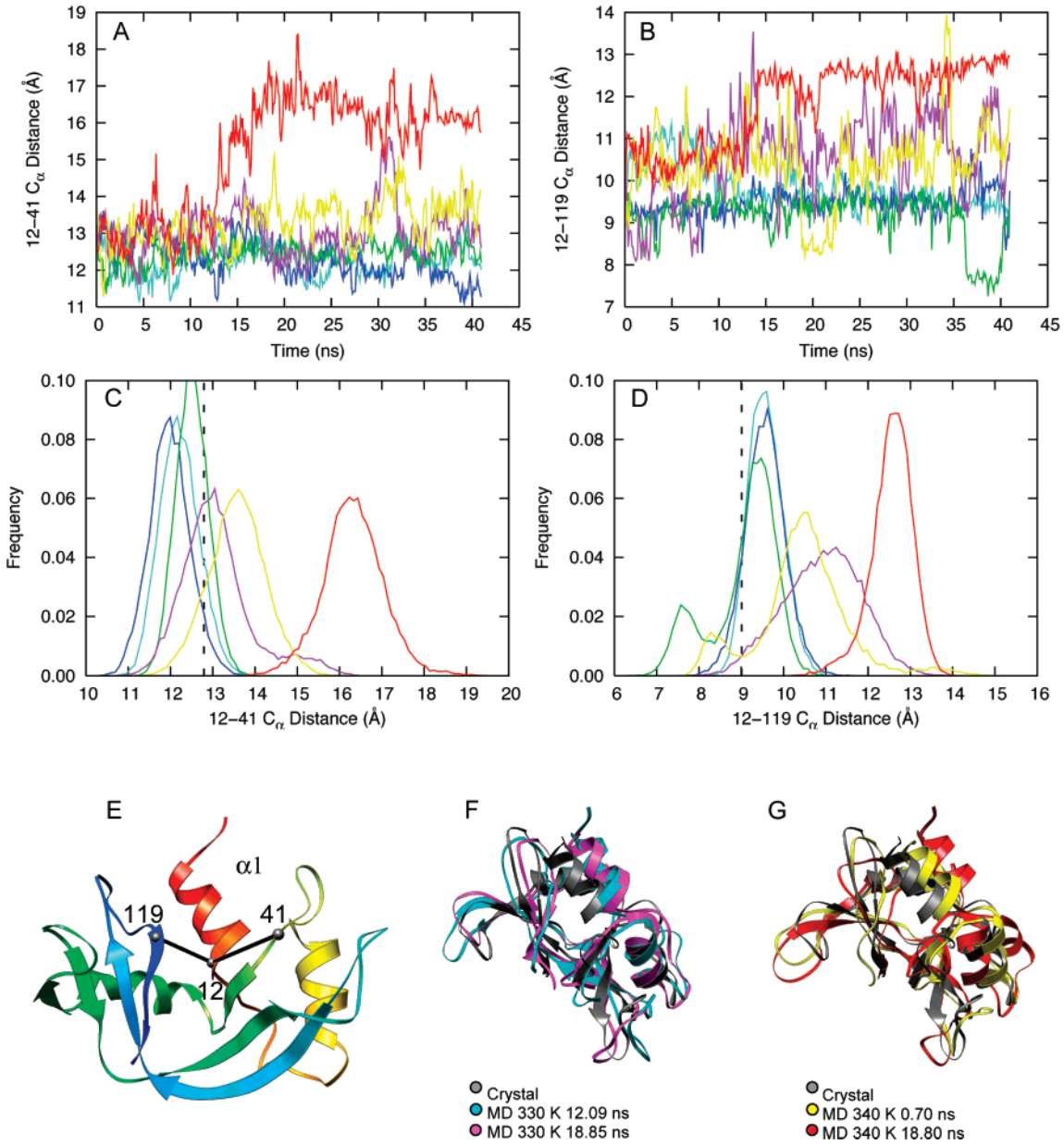


FIGURE 8: Motion of α1 disrupting the active site. (A and C) Distances between $C_\alpha$ atoms of His 12 and Lys 41 and (B and D) distances between $C_\alpha$ atoms of His 12 and His 119: cyan, 278 K; blue, 298 K; green, 310 K; magenta, 320 K; yellow, 330 K; and red, 340 K. For clarity, the data in panels A and C have been smoothed over a 100 ps sliding window. The histograms in panels B and D were calculated using the data from 20 to 41 ns of each simulation. (E) Structure of RNase A indicating the distances shown in panels A and C (black lines between gray spheres at the $C_\alpha$ positions). (F) Superposition of the starting structure and snapshots from simulations at 330 K, showing the motion of α1. The alignment was over all $C_\alpha$ atoms in the regular secondary structure in the crystal structure, excluding α1. (G) Superposition of the starting structure and snapshots from simulations at 340 K, showing the motion of α1.

region of the domain-swapped dimer of a variant of the human pancreatic enzyme adopts a $3_{10}$-helical conformation (*59*), there is no evidence of partial unfolding (such as dissociation of α1) under conditions where domain swapping occurs (*60*).

*Temperature-Induced Conformational Changes of RNase A. Contact Analysis. (i) Contact Density.* The difference contact density for the RNase A simulations is given in Figure 7. This quantity is equivalent to the average number of native contacts that a given residue loses during the simulation (see Methods). Some aspects of the pattern of loss of native contacts are similar at all temperatures. The C-terminus of α1, the buried face and C-terminus of α2, the buried face of α3, $\beta$1, and the α1−α2 and α2−$\beta$1 loops show slight changes at the three lowest temperatures. At the higher temperatures, native contacts are lost in the same regions, but the loss is more pronounced. For instance, the locations of lost native contacts in $\beta$4 (residues 80, 81, 83, and 85) and $\beta$5 (residue 101) are identical at all temperatures. Other changes appear only at the higher temperatures. In α1, in addition to a greater loss of native contacts at its C-terminus, the changes extend toward the N-terminus, especially Ala 5 and Phe 8. $\beta$2, $\beta$3, and $\beta$6 (which, with $\beta$7, make up the V1 arm of the V-shaped $\beta$-sheet structure) also show large losses in the number of native contacts only at the three highest temperatures.

Some of the high-temperature changes directly involve the active site, which is located in a groove formed by the two

arms of the V-shaped $\beta$-sheet structure (see Figure 1A). $\alpha$1 sits at one end of the groove. The catalytic His residues are contributed by $\alpha$1 (His 12) and $\beta$7 (His 119). Since $\beta$7 loses many of its hydrogen bonds to $\beta$6 at high temperature, it becomes more disordered. The large loss of native contacts to Ala 5 and Phe 8 is due to both changes in the conformation of residues 117−120 in $\beta$7 and a change in the relative orientation of $\alpha$1 and $\beta$7. Changes are reflected in the time course and distribution of distances across the active site (Figure 8A−D). The motion of $\alpha$1 is illustrated in Figure 8E−G. Its position relative to $\beta$1 and $\beta$7 fluctuates: at times it swings further out into solution, and at times it is pulled in the opposite direction to partially obstruct the active site groove. This motion changes the register of interactions such that Val 118, which interacts with Ala 5 in the crystal structure, moves to interact with Phe 8 (this change is most pronounced at 320 and 330 K). Phe 8, in turn, loses its native interactions with His 119 and Phe 120, although fluctuating contacts with these residues in nonnative conformations do occur. Further changes in the backbone of $\beta$7 lead to more disruption in the active site groove. Side chain motions also contribute. The Phe 120 side chain occasionally rotates upward to a position that partially fills the groove and blocks hydrogen bonding of substrate by its own backbone N atom. At 320 and 330 K, His 119 rotates rapidly, seldom maintaining its native interaction with Asp 121, its partner in the catalytic diad. At 340 K, His 119 rotates away from the active site to interact with residues in the $\beta$6−$\beta$7 loop, visiting an alternate conformation seen in the NMR structure and some crystal structures (*6*, *35*), as well as other conformations.

A recent study of global and local thermal unfolding in RNase A using Trp-containing mutants found that local unfolding (by Trp fluorescence) occurred 6−11 K lower than global unfolding (far-UV CD) for the F8W, Y92W, K104W, and Y115W mutants (*14*). Significant changes near Phe8 are seen in our 310, 320, and 330 K simulations. Smaller changes are seen at Lys 104, but the neighboring His 105 shows a significant loss of native contacts. Tyr 92 and Tyr 115 do not lose large numbers of native contacts in our simulation (Figure 7). These results suggest that at least some of the key features of local unfolding are reflected in our simulations.

*Effect of Temperature on Dynamics. (i) Backbone Fluctuations.* A similar pattern of flexibility is observed at all temperatures. As expected, the $C_\alpha$ rmsf (Figure 9A) indicates greater mobility in loop regions and greater stability of regular secondary structure elements. The pairwise correlation coefficients $R$ for $C_\alpha$ rmsf data between simulations at different temperatures range from 0.81 to 0.95. The correlation between simulation $C_\alpha$ rmsf and experimental $C_\alpha$ rmsf is 0.69−0.71 for the three lowest temperatures and 0.62−0.68 for the three highest. The greatest deviation from the crystallographic rmsf values is in $\beta$2 and $\beta$3 and the intervening loop (residues 61−78). In simulation, this loop is very dynamic, but in the crystal structure, the dynamics of this loop may be inhibited by crystal packing contacts (*7*). To further compare the flexibility in simulation to experimental *B*-factors, we calculated the $C_\alpha$ rmsf from the *B*-factors of 18 different unliganded crystal structures of RNase A. The one-standard-deviation limits of this set are shown in Figure 9A (dotted gray lines). Our simulation values generally fall within this range except for the termini

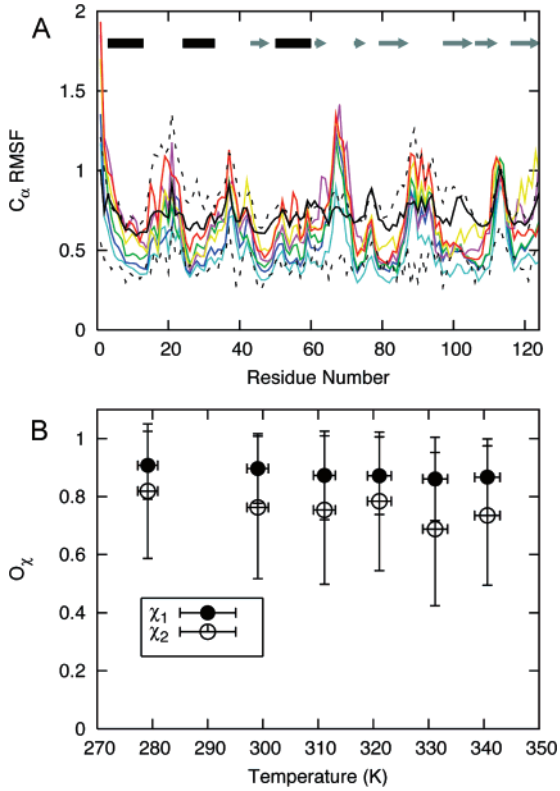


FIGURE 9: Dynamics of RNase A in simulation. (A) $C_\alpha$ rmsfs calculated from 20 to 41 ns: cyan, 278 K; blue, 298 K; green, 310 K; magenta, 320 K; orange, 330 K; red, 340 K; and solid black, *B*-factors calculated from the 1KF5 crystal structure. Dashed lines are plus or minus one standard deviation from the average rmsf values of a set of 18 ligand-free crystal structures of RNase A. (B) Side chain dihedral angle order parameters $O_\chi$ for $\chi_1$ ($C_\alpha$−$C_\beta$) and $\chi_2$ ($C_\beta$−$C_\gamma$) angles.

and residues 61−74 ($\beta$2, $\beta$3, and the intervening loop). Merlino et al. (*26*) also noted large fluctuations in this region in their simulation study.

The average $C_\alpha$ rmsf varies approximately linearly with an increase in temperature (linear regression slope, 0.0043 Å/K, $R$ = 0.988), with greater slopes for loops and termini. Converted to *B*-factor units, this value becomes 0.14 Å$^2$/K, which agrees reasonably well with the value of 0.064 Å$^2$/K determined by crystallography (*61*). The slope of individual rmsf values varies about the mean value given above. More than half of the residues have a strongly linear trend ($R \geq 0.9$). Interestingly, residues in $\alpha$1 show a sharp, discontinuous increase in $C_\alpha$ rmsf (0.17−0.27 Å) between 310 and 320 K.

*(ii) Side Chain Dynamics.* To measure side chain dynamics, we used the side chain dihedral order parameter $O_\chi$. This parameter is a measure of the persistence of the orientation of the bond vector, with a value of 1 meaning completely ordered and a value of zero meaning completely disordered. The $O_\chi$ values from the simulations (averaged over all residues) decrease linearly with temperature, indicating that side chains become more dynamic as the temperature increases, as expected. On average, $O_{\chi_1}$ was higher than $O_{\chi_2}$, indicating that $C_\alpha$−$C_\beta$ bonds are more rigid than $C_\beta$−$C_\gamma$ bonds. The average side chain order parameter varies approximately linearly with temperature (Figure 9B). There is no evidence for a global dynamic transition analogous to the conformational transition discussed above.

The observed trends in dynamic properties relating to backbone ($C_\alpha$ rmsf) and side chain ($O_\chi$) motions are linear when averaged over all residues. Per-residue $C_\alpha$ rmsf shows a clear transition only for a few residues in α1. These findings suggest that the thermal pretransition of RNase A may be mainly a conformational change, not a dynamic one. The mobility of α1 can be seen as either a consequence or a cause of its altered conformation.

*Temperature-Dependent Native States.* A recent simulation study of chymotrypsin inhibitor 2 (CI2) suggests that the CI2 N′ state is nativelike but expanded (*4*). The CI2 N′ state preserves the overall native topology and many native contacts, although some contact distances are increased. Many nonnative contacts are also present. The putative CI2 N′ state is the native state in the sense that it is folded and it is the stable conformation in the simulation. However, in the strict sense of biological activity, the CI2 N′ state may be nonnative, since the active site loop is distorted.

Similar properties are also found in the high-temperature RNase A simulations in this work. As in Figure 1, the conformations of RNase A in our simulations at high temperature, especially at 320 and 330 K, are nativelike, with the $C_\alpha$ rmsd from the starting structure being <5 Å. The conformations seen at high temperatures maintain ∼90% of the native contacts (Figure 3E). As with CI2, if the contact definition distance is extended to 8 Å, even more of the native contacts are preserved (not shown). Similarly, the native secondary structural elements are largely maintained at high temperature (Figure 5). The exceptions occur at 340 K, which is at or near the $T_m$, or in elements (such as β1) that may be involved in the pretransition. Where secondary structure is disrupted, the conformation is typically maintained even though hydrogen bonding is lost (see above).

In the putative N′ state of CI2, the active site loop is disrupted compared with the native, biologically active conformation. Similarly, the active site of RNase A is perturbed in our simulations, largely by the motions of α1, β1, and β7. This agrees with the observed decline in RNase A activity toward 2′,3′-cyclic cytidine monophosphate above 320 K (*21*), and with the general conception that enzyme active sites are disrupted at denaturant concentrations lower than those required for global unfolding events (*62*).

The N′ state may be considered an ensemble in which many higher-energy microstates are populated relative to the native (N) ensemble, which could lead to a shift in the distribution of conformational properties with an increase in temperature. Such a scenario was observed for alternative conformations of cytochrome $b_5$ by both simulation and experiment (*63*). In this view, the underlying energy landscape could be independent of temperature. A temperature-independent energy landscape is supported by our simulation studies of CI2 at a variety of temperatures (*64*). That is, unfolding accelerates with an increase in temperature, but the pathway of unfolding is independent of temperature. Alternatively, the N′ state may arise from a shift in the energy minimum with an increase in temperature. In other words, the N′ is the N state at elevated temperature, and the landscape itself changes. This idea was put forward by Leeson et al. (*3*) to explain the nonexponential unfolding kinetics of cold shock protein A at high temperature. It will be difficult to distinguish between these models experimentally, because the spectroscopic signals of the N′ state may closely resemble that of the N state. For example, the fluorescent probe Trp 5 of CI2 is buried in its N′ state as it is in N.

## CONCLUSIONS

The existence of a thermal "pretransition" around 320 K in RNase A unfolding is well-documented in the literature, but the exact nature of the structural changes that occur during this pretransition is the subject of active study. Structural properties from our six simulations of RNase A at temperatures up to the $T_m$ also indicate the presence of a conformational transition between 310 and 320 K. Our simulation results suggest that the largest structural changes occur in the β-sheet, particularly strands 1 and 7. α1 does not unfold, but it does begin to pull away from the β-sheet core. This result, together with the observation of a nonnative helix (residues 15−20) at 330−340 K, echoes the conclusions of prior MD work (*34*) in suggesting a pathway for the formation of the N-terminal domain-swapped dimer. The extent and nature of the conformational changes observed in our simulations are in agreement with those expected for the high-temperature nativelike N′ state.

In contrast with the sharp change in conformational properties, global dynamic properties of RNase A vary linearly with temperature. If this finding is general, it has important implications for theories relating protein flexibility to enzyme function. If putative functionally important dynamic changes are subtle and local, as are the changes in RNase A α1 in this work, an understanding of such motions requires techniques capable of atomic resolution.

## ACKNOWLEDGMENT

We thank Alex Scouras for assistance in preparing Figure 5 and Alex Scouras, Darwin Alonso, and David Beck for helpful discussions and technical assistance, William Parson for reading the manuscript, and Luciana Esposito for help with histidine tautomer assignments.

## SUPPORTING INFORMATION AVAILABLE

Interatomic distances from MD simulations illustrating the conformational changes occurring in the pretransition (Figure S1). This material is available free of charge via the Internet at http://pubs.acs.org.

## REFERENCES

1. Lu, H. P., Xun, L. Y., and Xie, X. S. (1998) Single-molecule enzymatic dynamics, *Science 282*, 1877−1882.
2. Santoro, M. M., and Bolen, D. W. (1988) Unfolding free energy changes determined by the linear extrapolation method. 1. Unfolding of phenylmethanesulfonyl-α-chymotrypsin, *Biochemistry 27*, 8063−8068.
3. Leeson, D. T., Gai, F., Rodriguez, H. M., Gregoret, L. M., and Dyer, R. B. (2000) Protein folding and unfolding on a complex energy landscape, *Proc. Natl. Acad. Sci. U.S.A. 97*, 2527−2532.
4. Day, R., and Daggett, V. (2007) Direct Observation of Microscopic Reversibility in Single-molecule Protein Folding, *J. Mol. Biol. 366*, 677−686.
5. Wlodawer, A. (1980) Studies of Ribonuclease-A by X-ray and Neutron Diffraction, *Acta Crystallogr. B36*, 1826−1831.
6. Santoro, J., Gonzalez, C., Bruix, M., Neira, J. L., Nieto, J. L., Herranz, J., and Rico, M. (1993) High-Resolution 3-Dimensional Structure of Ribonuclease-A in Solution by Nuclear-Magnetic-Resonance Spectroscopy, *J. Mol. Biol. 229*, 722−734.

7. Berisio, R., Sica, F., Lamzin, V. S., Wilson, K. S., Zagari, A., and Mazzarella, L. (2002) Atomic resolution structures of ribonuclease A at six pH values, *Acta Crystallogr. D58*, 441−450.
8. Sasisanker, P., Oleinikova, A., Weingartner, H., Ravindra, R., and Winter, R. (2004) Solvation properties and stability of ribonuclease A in normal and deuterated water studied by dielectric relaxation and differential scanning/pressure perturbation calorimetry, *Phys. Chem. Chem. Phys. 6*, 1899−1905.
9. Stelea, S. D., Pancoska, P., Benight, A. S., and Keiderling, T. A. (2001) Thermal unfolding of ribonuclease A in phosphate at neutral pH: Deviations from the two-state model, *Protein Sci. 10*, 970−978.
10. Tsong, T. Y., Hearn, R. P., Wrathall, D. P., and Sturtevant, J. M. (1970) A Calorimetric Study of Thermally Induced Conformational Transitions of Ribonuclease-A and Certain of Its Derivatives, *Biochemistry 9*, 2666−2677.
11. Liu, Y. F., and Sturtevant, J. M. (1996) The observed change in heat capacity accompanying the thermal unfolding of proteins depends on the composition of the solution and on the method employed to change the temperature of unfolding, *Biochemistry 35*, 3059−3062.
12. Neira, J. L., Sevilla, P., Menendez, M., Bruix, M., and Rico, M. (1999) Hydrogen exchange in ribonuclease A and ribonuclease S: Evidence for residual structure in the unfolded state under native conditions, *J. Mol. Biol. 285*, 627−643.
13. Matheson, R. R., and Scheraga, H. A. (1979) Steps in the Pathway of the Thermal Unfolding of Ribonuclease A. A Non-specific Photochemical Surface-Labeling Study, *Biochemistry 18*, 2437−2445.
14. Navon, A., Ittah, V., Laity, J. H., Scheraga, H. A., Haas, E., and Gussakovsky, E. E. (2001) Local and Long-Range Interactions in the Thermal Unfolding Transition of Bovine Pancreatic Ribonuclease A, *Biochemistry 40*, 93−104.
15. Burgess, A. W., and Scheraga, H. A. (1975) A hypothesis for the pathway of the thermally-induced unfolding of bovine pancreatic ribonuclease, *J. Theor. Biol. 53*, 403.
16. Wang, L. X., Wu, Y. Q., and Meersman, F. (2006) Clarification of the thermally-induced pretransition of ribonuclease A in solution by principal component analysis and two-dimensional correlation infrared spectroscopy, *Vib. Spectrosc. 42*, 201−205.
17. Wang, L. X., Wu, Y. Q., and Meersman, F. (2006) Two-dimensional correlation infrared spectroscopic study on the conformational changes occurring in the thermally induced pretransition of ribonuclease A, *J. Mol. Struct. 799*, 85−90.
18. Zhang, J., He, H. W., Wang, Q., and Yan, Y. B. (2006) Sequential events in ribonuclease A thermal unfolding characterized by two-dimensional infrared correlation spectroscopy, *Protein Pept. Lett. 13*, 33−40.
19. Schultz, C. P., Fabian, H., and Mantsch, H. H. (1998) Two-dimensional mid-IR and near-IR correlation spectra of ribonuclease A: Using overtones and combination modes to monitor changes in secondary structure, *Biospectroscopy 4*, S19−S29.
20. Chen, M. C., and Lord, R. C. (1976) Laser-Excited Raman-Spectroscopy of Biomolecules. 9. Laser Raman Spectroscopic Studies of Thermal Unfolding of Ribonuclease-A, *Biochemistry 15*, 1889−1897.
21. Arnold, U., and Ulbrich-Hofmann, R. (2000) Differences in the Denaturation Behavior of Ribonuclease A Induced by Temperature and Guanidine Hydrochloride, *J. Protein Chem. 19*, 345−352.
22. Zhang, J., Peng, X., Jonas, A., and Jonas, J. (1995) NMR Study of the Cold, Heat, and Pressure Unfolding of Ribonuclease A, *Biochemistry 34*, 8631−8641.
23. Howarth, O. W., and Lian, L. Y. (1984) Ribonuclease-A: C-13 Nuclear Magnetic-Resonance Assignments, Binding-Sites, and Conformational Flexibility, *Biochemistry 23*, 3515−3521.
24. Wang, A., Robertson, A. D., and Bolen, D. W. (1995) Effects of a Naturally-Occurring Compatible Osmolyte on the Internal Dynamics of Ribonuclease-A, *Biochemistry 34*, 15096−15104.
25. Merlino, A., Vitagliano, L., Ceruso, M. A., and Mazzarella, L. (2004) Dynamic properties of the N-terminal swapped dimer of ribonuclease A, *Biophys. J. 86*, 2383−2391.
26. Merlino, A., Vitagliano, L., Ceruso, M. A., Di Nola, A., and Mazzarella, L. (2002) Global and Local Motions in Ribonuclease A: A Molecular Dynamics Study, *Biopolymers 65*, 274−283.
27. Merlino, A., Ceruso, M. A., Vitagliano, L., and Mazzarella, L. (2005) Open Interface and Large Quaternary Structure Movements in 3D Domain Swapped Proteins: Insights from Molecular Dynamics Simulations of the C-Terminal Swapped Dimer of Ribonuclease A, *Biophys. J. 88*, 2003−2012.
28. Nadig, G., Ratnaparkhi, G. S., Varadarajan, R., and Vishveshwara, S. (1996) Dynamics of ribonuclease A and ribonuclease S: Computational and experimental studies, *Protein Sci. 5*, 2104−2114.
29. Nadig, G., and Vishveshwara, S. (1997) Effects of Substrate Binding on the Dynamics of RNase A: Molecular Dynamics Simulations of UpA Bound and Native RNase A, *Biopolymers 42*, 505−520.
30. Sanjeev, B. S., and Vishveshwara, S. (2004) Protein-Water Interactions in Ribonuclease A and Angiogenin: A Molecular Dynamics Study, *Proteins: Struct., Funct., Bioinf. 55*, 915−923.
31. Madhusudhan, M. S., and Vishveshwara, S. (2001) Deducing Hydration Sites of a Protein from Molecular Dynamics Simulations, *J. Biomol. Struct. Dyn. 19*, 105−114.
32. Straub, J. E. (1994) Simulations Analysis of the Binding Interactions in the RNase A/3′-UMP Enzyme-Product Complex as a Function of pH, *J. Am. Chem. Soc. 116*, 2591−2599.
33. Brunger, A. T., Brooks, C. L., and Karplus, M. (1985) Active site dynamics of ribonuclease, *Proc. Natl. Acad. Sci. U.S.A. 82*, 8458−8462.
34. Esposito, L., and Daggett, V. (2005) Insight into ribonuclease A domain swapping by molecular dynamics unfolding simulations, *Biochemistry 44*, 3358−3368.
35. Berisio, R., Lamzin, V. S., Sica, F., Wilson, K. S., Zagari, A., and Mazzarella, L. (1999) Protein titration in the crystal state, *J. Mol. Biol. 292*, 845−854.
36. Beck, D. A. C., and Daggett, V. (2004) Methods for molecular dynamics simulations of protein folding/unfolding in solution, *Methods 34*, 112−120.
37. Levitt, M., Hirshberg, M., Sharon, R., Laidig, K., and Daggett, V. (1997) Calibration and Testing of a Water Model for Simulation of the Molecular Dynamics of Proteins and Nucleic Acids in Solution, *J. Phys. Chem. B 101*, 5051−5056.
38. Levitt, M., Hirshberg, M., Sharon, R., and Daggett, V. (1995) Potential energy function and parameters for simulations of the molecular dynamics of proteins and nucleic acids in solution, *Comput. Phys. Commun. 91*, 215−231.
39. Gerstein, M., Tsai, J., and Levitt, M. (1995) The Volume of Atoms on the Protein Surface: Calculated from Simulation, Using Voronoi Polyhedra, *J. Mol. Biol. 249*, 955−966.
40. Kell, G. S. (1967) Precise Representation of Volume Properties of Water at 1 Atmosphere, *J. Chem. Eng. Data 12*, 66−69.
41. Haar, L., Gallagher, J. S., and Kell, G. S. (1984) Thermodynamic and transport properties and computer programs for vapor and liquid states of water in SI units, *NBS/NRC Steam Tables*, Hemisphere Publishing Group: Washington, D.C.
42. Yee, D. P., and Dill, K. A. (1993) Families and the Structural Relatedness among Globular Proteins, *Protein Sci. 2*, 884−899.
43. Wong, K. B., and Daggett, V. (1998) Barstar has a highly dynamic hydrophobic core: Evidence from molecular dynamics simulations and nuclear magnetic resonance relaxation data, *Biochemistry 37*, 11182−11192.
44. Kabsch, W., and Sander, C. (1983) Dictionary of Protein Secondary Structure: Pattern Recognition of Hydrogen-Bonded and Geometrical Features, *Biopolymers 22*, 2577−2637.
45. Lee, B., and Richards, F. M. (1971) Interpretation of Protein Structures: Estimation of Static Accessibility, *J. Mol. Biol. 55*, 379.
46. Pettersen, E. F., Goddard, T. D., Huang, C. C., Couch, G. S., Greenblatt, D. M., Meng, E. C., and Ferrin, T. E. (2004) UCSF chimera: A visualization system for exploratory research and analysis, *J. Comput. Chem. 25*, 1605−1612.
47. Wlodawer, A. (1986) Comparison of Two Independently Refined Models of Ribonuclease-A, *Acta Crystallogr. B42*, 379−387.
48. Gilliland, G. L. (1997) Crystallographic Studies of Ribonuclease Complexes, in *Ribonucleases: Structure and Function* (D'Alessio, G., and Riordan, J. F., Eds.) Academic Press, New York.
49. Vitagliano, L., Adinolfi, S., Riccio, A., Sica, F., Zagari, A., and Mazzarella, L. (1998) Binding of a substrate analog to a domain swapping protein: X-ray structure of the complex of bovine seminal ribonuclease with uridylyl(2′,5′)adenosine, *Protein Sci. 7*, 1691−1699.
50. Lacroix, E., Viguera, A. R., and Serrano, L. (1998) Elucidating the folding problem of α-helices: Local motifs, long-range electrostatics, ionic-strength dependence and prediction of NMR parameters, *J. Mol. Biol. 284*, 173−191.
51. Munoz, V., and Serrano, L. (1997) Development of the multiple sequence approximation within the AGADIR model of α-helix

formation: Comparison with Zimm-Bragg and Lifson-Roig formalisms, *Biopolymers 41*, 495−509.
52. Munoz, V., and Serrano, L. (1995) Elucidating the Folding Problem of Helical Peptides Using Empirical Parameters. 2. Helix Macrodipole Effects and Rational Modification of the Helical Content of Natural Peptides, *J. Mol. Biol. 245*, 275−296.
53. Munoz, V., and Serrano, L. (1995) Elucidating the Folding Problem of Helical Peptides Using Empirical Parameters. 3. Temperature and pH Dependence, *J. Mol. Biol. 245*, 297−308.
54. Munoz, V., and Serrano, L. (1994) Elucidating the Folding Problem of Helical Peptides Using Empirical Parameters, *Nat. Struct. Biol. 1*, 399−409.
55. Liu, Y. S., Hart, P. J., Schlunegger, M. P., and Eisenberg, D. (1998) The crystal structure of a 3D domain-swapped dimer of RNase A at a 2.1-angstrom resolution, *Proc. Natl. Acad. Sci. U.S.A. 95*, 3437−3442.
56. Gotte, G., Vottariello, F., and Libonati, M. (2003) Thermal aggregation of ribonuclease A: A contribution to the understanding of the role of 3D domain swapping in protein aggregation, *J. Biol. Chem. 278*, 10763−10769.
57. Merlino, A., Vitagliano, L., Sica, F., Zagari, A., and Mazzarella, L. (2004) Population shift vs induced fit: The case of bovine seminal ribonuclease swapping dimer, *Biopolymers 73*, 689−695.
58. Sica, F., Di Fiore, A., Merlino, A., and Mazzarella, L. (2004) Structure and Stability of the Non-covalent Swapped Bovine Seminal Ribonuclease, *J. Biol. Chem. 279*, 36753−36760.
59. Canals, A., Pous, J., Guasch, A., Benito, A., Ribo, M., Vilanova, M., and Coll, M. (2001) The structure of an engineered domain-swapped ribonuclease dimer and its implications for the evolution of proteins toward oligomerization, *Structure 9*, 967−976.
60. Rodriguez, M., Benito, A., Ribo, M., and Vilanova, M. (2006) Characterization of the dimerization process of a domain-swapped dimeric variant of human pancreatic ribonuclease, *FEBS J. 273*, 1166−1176.
61. Tilton, R. F., Dewan, J. C., and Petsko, G. A. (1992) Effects of Temperature on Protein Structure and Dynamics: X-ray Crystallographic Studies of the Protein Ribonuclease-A at Nine Different Temperatures From 98 to 320 K, *Biochemistry 31*, 2469−2481.
62. Tsou, C.-L. (1998) Active Site Flexibility in Enzyme Catalysis, *Ann. N.Y. Acad. Sci. 864*, 1.
63. Storch, E. M., Daggett, V., and Atkins, W. M. (1999) Engineering Out Motion: Introduction of a de Novo Disulfide Bond and a Salt Bridge Designed To Close a Dynamic Cleft on the Surface of Cytochrome $b_5$, *Biochemistry 38*, 5054−5064.
64. Day, R., Bennion, B. J., Ham, S., and Daggett, V. (2002) Increasing temperature accelerates protein unfolding without changing the pathway of unfolding, *J. Mol. Biol. 322*, 189−203.
65. Scouras, A. D., and Daggett, V. (2007) Species Variation in $PrP^{Sc}$ Protofibril Models, *J. Mater. Sci.* (in press).

BI701565B